Document downloaded from:

http://hdl.handle.net/10251/201165

This paper must be cited as:

Martínez-Turégano, J.; Añó Villalba, SC.; Bernal-Perez, S.; Peña, R.; Blasco-Gimenez, R. (2020). Small-signal stability and fault performance of mixed grid forming and grid following offshore wind power plants connected to a HVDC-diode rectifier. IET Renewable Power Generation. 14(12):2166-2175. https://doi.org/10.1049/iet-rpg.2019.1264

The final publication is available at

https://doi.org/10.1049/iet-rpg.2019.1264

Copyright Institution of Electrical Engineers

Additional Information

ISSN
doi:10.1049/iet-rpg.2019.1264

Small-signal Stability and Fault Performance of Mixed Grid Forming and Grid Following Offshore Wind Power Plants Connected to a HVDC-Diode Rectifier

J. Martínez-Turégano[1] *S. Añó-Villalba*[1] *S. Bernal-Perez*[1] *R. Peña*[2] *R. Blasco-Gimenez*[1]

[1] *Universitat Politècnica de València, Spain*
[2] *Universidad de Concepción, Chile*
* *E-mail: jaumartu@upv.es*

Abstract: This paper aims at validating the simultaneous operation of grid following and grid forming wind power plants when connected to a common Diode Rectifier based HVDC link. The controllers for both grid forming and grid following wind turbines include fault-ride-through capability with soft restoration of the off-shore ac-grid. Current and voltage controllers are developed in the stationary $\alpha\beta$ reference frame. The presented control and soft restoration strategies are based on local measurements only and do not require communication between wind turbine generators. The small signal stability analysis of the mixed system in multiple d-q axis using detailed string models is carried out in order to show the sensitivity to grid following PLL gains and to grid forming droop gains. Interoperability between grid forming and grid following wind turbines during transients is shown by means of detailed simulation during symmetric faults in different locations of the off-shore grid.

1 Introduction

The use of HVDC Diode Rectifier (DR) stations has been proposed by the authors as a technical solution for a significant cost reduction for the grid connection of distant off-shore wind farms (OWFs), while increasing the efficiency and robustness of the overall system [1–5]. It is claimed by Siemens that the use of HVDC diode rectifier stations can lead to up to a 30% cost reduction for the electrical connection of large off-shore wind power plants (WPP) [6, 7].

However, as the DR station is a passive converter, wind turbine generators (WTGs) are required to create the off-shore ac-grid, and control the power delivered through the HVDC link. Several control strategies have been proposed to such avail [1–3, 6–12]. These grid forming control strategies for DR connected WTGs are based on the fact that off-shore ac-grid voltage is effectively capped by the HVDC-link voltage when the diode rectifiers are conducting and also on the fact that off-shore ac-grid frequency has a strong dependency on the reactive power delivered by the WTGs due to the large system capacitance from cables and capacitor banks [1].

Current industrial standard WTGs are grid following and hence cannot be used directly for diode rectifier (DR) connection. Solutions allowing operation of standard WTGs with a diode rectifier connection are of particular industrial importance, as it would allow the DR connection of existing certified grid following WTGs from different manufacturers. In [8], a series connection of the Diode Rectifier and a voltage source converter for the HVDC-link has been proposed which allows the use of standard WTGs, at the expense of needing additional equipment. The connection of standard grid following WTGs to Line Commutated Converters (LCC) is also shown in [13], however this solution required an additional STATCOM and a controlled LCC rectifier.

None of the previous published work addressed the issue of joint connection of grid forming and grid following wind turbine generators (WTGs) to HVDC Diode Rectifier stations. To validate the technical feasibility and interoperability of the HVDC DC connection of mixed grid forming and grid following OWFs, this paper includes the small signal stability and fault-ride-through performance of the proposed system. The study of such a system has been carried out by means of detailed PSCAD simulations.

The proposed control strategy for both grid forming and grid following WTGs does not require communication for normal and fault operation. Moreover, the presented strategy shows an excellent behaviour of the complete system during off-shore ac-grid short-circuits, again, without requiring communication between WTGs.

This paper is organized in four sections and includes the description of the system to be analysed, a description of both grid forming and grid following control strategies, the stability analysis of the detailed system, a fault-ride-through study and the corresponding discussion and conclusions.

2 System Description

Fig. 1 shows the diagram of the complete system, based on the distributed Diode Rectifier Station proposed in [6]. Therefore, three 400 MW off-shore wind power plants have been considered, connected via a diode-based HVDC link to a full-bridge on-shore Modular Multi-level Converter (MMC). Each OWF consists of fifty Type-4 8 MW rated WTGs. Each OWF is modeled by considering one detailed string of 9 WTGs, whereas the rest of the strings are modeled by using an aggregated wind turbine for each string, as shown in Fig. 1. WTGs have been aggregated as per [14]. Therefore, the considered system shows a great level of granularity, so results can be obtained at the wind turbine and string levels, at a reasonable computational cost. Wind turbine transformer models consider saturation.

The DR converter consists of six 12-pulse diode rectifier units (DRU) of 200 MW each, parallel connected on the ac-side, series connected on the dc-side and distributed in three platforms [6], albeit the installation in a single platform is also possible.

In this topology, each off-shore wind farm OWF-i ($i = 1, 2, 3$) is connected to the corresponding DRU platform-i. An ac-ring bus connects the ac-side collector buses of the three DRU platforms. Each platform includes the corresponding ac and dc filters. The ac-grid is modelled using lumped π-parameters.

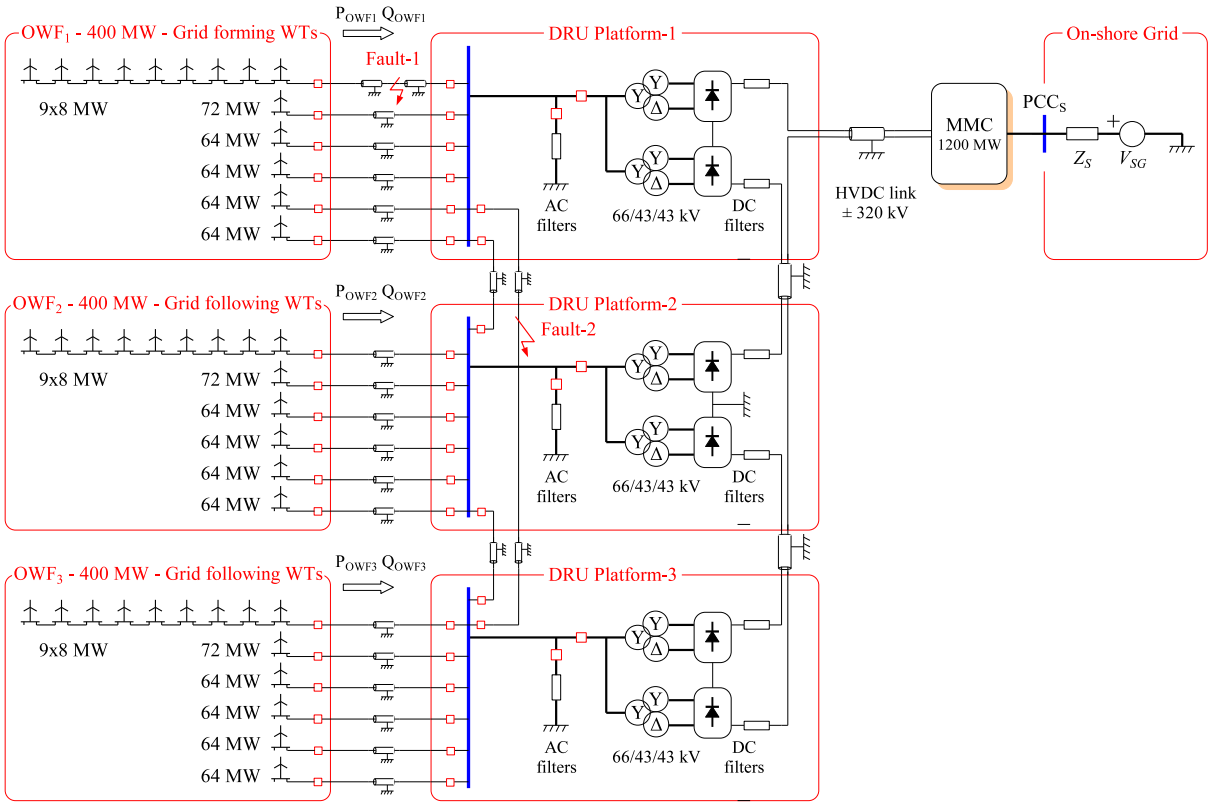

Fig. 1: OWFs connected to the on-shore ac-grid via a diode-based HVDC link. Grid forming WTGs: OWF_1; grid following WTGs: OWF_2 and OWF_3.

In the considered system, OWF_1 consists of DR-capable grid forming WTGs, whereas OWF_2 and OWF_3 consist of standard grid following WTGs.

The HVDC submarine cable connects the dc-side of the DRU platforms to the on-shore MMC converter, which exports the energy to the on-shore ac-grid. The HVDC cable is modelled using a distributed model with frequency dependent parameters. The grid forming WTGs could be used for black-starting the complete system provided that the WTG has an energy storage system that allows the WTG to yaw to the wind and that there is enough wind to compensate system losses.

System parameter values are shown in the Appendix 1.

3 Control Strategy

This section presents the proposed control strategies for DR-enabled grid forming and traditional grid following WTGs. Both control strategies are implemented as decentralised controllers using only local signals for feedback. Therefore, communications between WTGs are not required (other than general wind farm controller communications). Moreover, both control strategies include fault-ride-through capability.

The on-shore MMC controls the dc-voltage of the HVDC link and the reactive power injected to the on-shore ac-grid, albeit the MMC responses are not analyzed in this paper.

Control parameter values are shown in Appendix 1.

3.1 Grid Following Wind Turbines

Fig. 2 shows the control strategy used for the grid following WTGs (blocks labeled (1) and (2) are part of the fault-ride-through strategy and are described in section 5.1). The grid following control consists of standard cascaded control loops, the inner loop controlling active and reactive currents (I_{W_d}, I_{W_q}), whereas the outer loop controls the back-to-back converter DC-link voltage (E_B) and the WTG reactive power (Q_{WT}) [15]. A PLL is used to provide grid synchronization. Additionally, the control strategy includes a fault detection algorithm for fault-ride-through operation using the grid admittance Y_T seen by the WTG. A more detailed description of the controllers is included as follows.

3.1.1 Current Control: Standard P+R $\alpha\beta$ stationary frame current controllers have been used for both grid following and grid forming controllers (Figs. 2 and 3):

$$V_{W\alpha\beta} = R_W I_{W\alpha\beta} + L_W \frac{dI_{W\alpha\beta}}{dt} + V_{C\alpha\beta} \tag{1}$$

where L_W and R_W are the parameters of the choke in Fig. 2, V_W is the voltage applied by the WTG inverter, and I_W is the current through the choke.

From (1), the grid side converter current $I_{W\alpha\beta}$ is controlled by means of stationary frame proportional-resonant controllers (PR) with a weighed feed-forward voltage term. The weighted voltage feed-forward term improves controller performance, particularly during faults [15, 16]. The output of the regulator $V^*_{W\alpha\beta}$ is:

$$V^*_{W\alpha\beta}(s) = G_{PR,I}(s)(I^*_{W\alpha\beta}(s) - I_{W\alpha\beta}(s)) + K_V V_{C\alpha\beta}(s) \tag{2}$$

where K_V is the V_W feedforward gain and $G_{PR,I}$ is the current PR controller [17, 18]:

$$G_{PR,I}(s) = K_{P,I} + \frac{K_{R,I} \cdot s}{s^2 + \omega_0^2} \tag{3}$$

where $K_{P,I}$ and $K_{R,I}$ are the proportional and resonant parameters of the PR controller.

The PR controller has been designed by stationary frame transformation of an equivalent d-q PI controller based on the synchronous plant equivalent of (1) [15, 19]. The controller is designed in order to achieve a bandwidth of 180 Hz. Clearly, this bandwidth is compatible with the considered 4 kHz grid-side converter switching frequency.

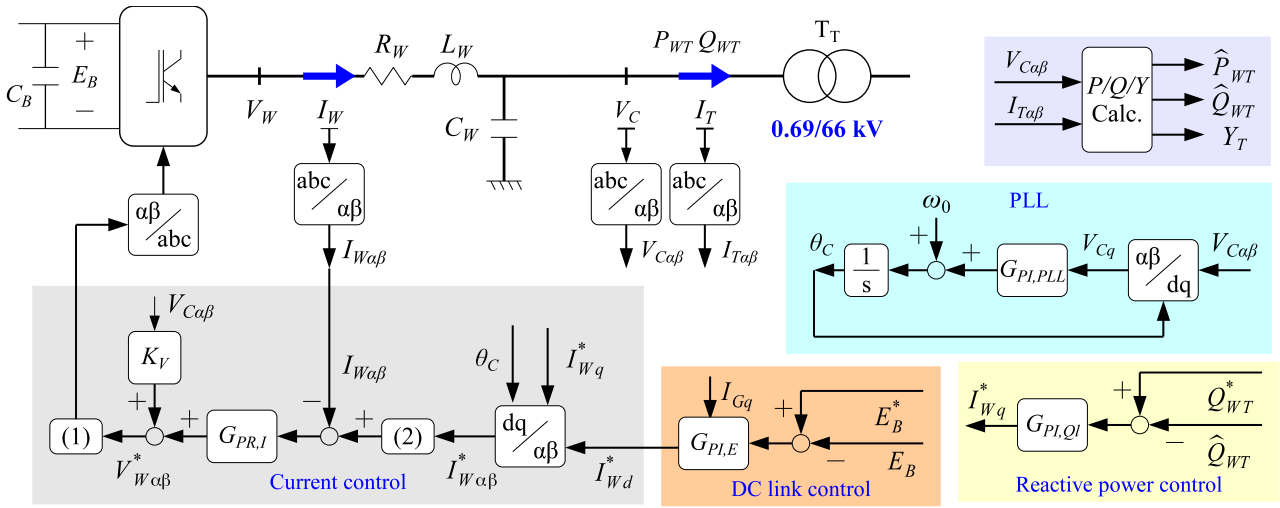

Fig. 2: Control strategies for grid following WTGs.

3.1.2 DC voltage control: The DC voltage of the back-to-back converter of the WTG is controlled by the front-end converter. This controller calculates the direct current reference $I^*_{W_d}$. Neglecting R_W losses, dc-link voltage dynamics can be expressed as:

$$C_B \frac{d}{dt} E_B = \frac{3}{2\sqrt{2}} (m_{GSC} I_{W_d} - m_{MSC} I_{G_q}) \tag{4}$$

where C_B is the DC-link capacitance and m_{GSC} and m_{MSC} are the PWM modulation indexes for grid-side and machine-side converters, respectively.

The voltage controller is based on a PI regulator. The output of the regulator I^*_{Wd} is

$$I^*_{Wd}(s) = G_{PI,E_B}(s)(E^*_B(s) - E_B(s)) + \frac{m_{MSC}}{m_{GSC}} I_{G_q} \tag{5}$$

where $G_{PI,E_B}(s)$ is

$$G_{PI,E_B}(s) = K_{P,E_B} + \frac{K_{I,E_B}}{s} \tag{6}$$

3.1.3 PLL: The grid following controller includes a PLL in order to allow the synchronization of the WTGs to the ac-grid. Additionally, the PLL helps the WTGs to be synchronized during faults. The implemented PLL is based on the well-known SRF-PLL [9, 20, 21]. So, the phase angle of V_C is calculated as

$$\theta_C(s) = \left(\left(K_{P,PLL} + \frac{K_{I,PLL}}{s} \right) (0 - V_{Cq}(s)) + \omega_0 \right) \frac{1}{s} \tag{7}$$

3.2 Grid Forming Controllers

Fig. 3 shows the control strategy used for the grid forming WTGs. The control strategy consists of cascaded controls for the wind turbine current I_W, ac-filter capacitor voltage V_C, and active and reactive powers P_{WT} and Q_{WT}. Additionally, the control strategy includes a fault detection algorithm for fault-ride-through operation using the grid admittance Y_T seen by the WTG. The description of the grid forming wind turbine controllers is included below.

3.2.1 Current Control Loops: The current control loops for the grid forming WTGs are exactly the same as the ones used for the grid following WTGs, i.e. PR controllers designed for a 180 Hz bandwidth including a weighted $V_{C\alpha\beta}$ feedforward term [15, 22].

3.2.2 Voltage Control: The wind turbine ac-filter capacitor voltage V_C dynamics can be expressed, in the stationary $\alpha\beta$ reference frame, as

$$C_W \frac{dV_{C\alpha\beta}}{dt} = I_{W\alpha\beta} - I_{T\alpha\beta} \tag{8}$$

Therefore, the voltage controller also is based on a PR regulator [15, 23]. The output of the regulator I^*_W is

$$I^*_{W\alpha\beta}(s) = G_{PR,V}(s)(V^*_{C\alpha\beta}(s) - V_{C\alpha\beta}(s)) \tag{9}$$

where $G_{PR,V}(s)$ is

$$G_{PR,V}(s) = K_{P,V} + \frac{K_{R,V} \cdot s}{s^2 + \omega_0^2} \tag{10}$$

The parameters of the voltage regulator have been obtained by designing a synchronous frame PI controller, aiming at a 40 Hz closed loop bandwidth, and transforming the parameters to obtain the equivalent stationary frame PR controller [15, 19].

3.2.3 Power Control: When the diode rectifier is conducting, the active power transmitted by the DRUs depends on the voltage levels of both off-shore ac-grid (V_{Fd}) and HVDC grid (V_{Rdc}) and on the equivalent impedance between these points, [24],

$$V_{Rdc0} - V_{Rdc} = \frac{3}{\pi} B\omega_0 L_{TR} I_{Rdc} + 2BL_{TR} \frac{dI_{Rdc}}{dt} \tag{11}$$

here $V_{Rdc0} = \frac{3\sqrt{6}}{\pi} BNV_{Fd}$, V_{Fd} is the off-shore ac-grid voltage magnitude, B is the number of rectifier bridges, N and L_{TR} are the diode rectifier transformer ratio and leakage reactance, respectively. In practice, the resistive term $R_{eq} = \frac{3}{\pi} B\omega_0 L_{TR}$ is relatively large, as the diode rectifier leakage reactance is around 0.18 pu.

Therefore, the active power sent by the OWF through the DRUs depends on the voltage levels of the off-shore ac-grid and the HVDC grid

$$P_{Rdc} = \frac{(V_{Rdc0} - V_{Rdc})\, V_{Rdc}}{R_{eq}} \tag{12}$$

A similar behaviour is shown in [25, 26] for a mostly resistive line impedance.

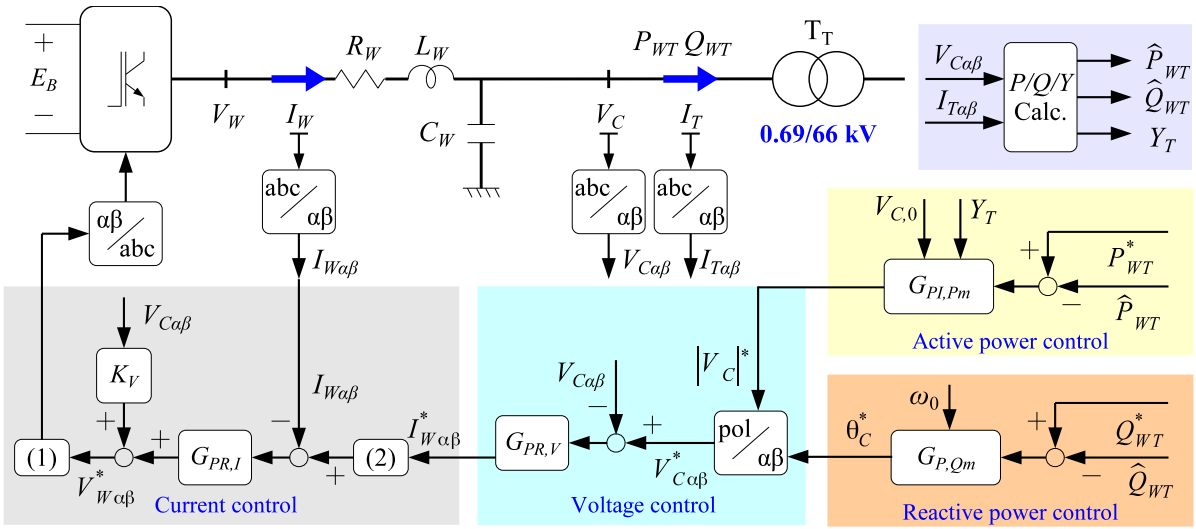

Fig. 3: Control strategies for grid forming WTGs.

Therefore, a decentralized P/V PI control and Q/θ droop control is proposed:

$$\left|V_C^*\right|(s) = \left(K_{P,Pm} + \frac{K_{I,Pm}}{s}\right)\left(P^*_{WT}(s) - \widehat{P}_{WT}(s)\right) \quad (13)$$

$$\theta^*_C(s) = K_{P,Qm}(Q^*_{WT}(s) - \widehat{Q}_{WT}(s)) + \frac{1}{s}\omega_0 \quad (14)$$

The parameters of the active and the reactive power control are designed in order to achieve a bandwidth of 8 Hz. Active and reactive powers measurements are first order filtered, with a cut-off frequency of 314.16 rad/s ($\widehat{P}_{WT}$ and $\widehat{Q}_{WT}$ in Fig. 3).

4 Decentralised Control Analysis

The controllers have been tuned assuming aggregated converters, therefore, this section includes the analysis of the complete system dynamic model, including local synchronouos frames of reference and local controllers. The model is developed considering complex variables and includes the stationary frame model of the electric system and the α-β part of the controllers:

$$\dot{x}^{\alpha\beta} = Ax^{\alpha\beta} + Bu^{\alpha\beta} \quad (15)$$

The control input $u_i^{\alpha\beta}$ is not calculated in fixed coordinates, but rather in local synchronous coordinates alined to angle θ_i:

$$u_i^{dq} = u_i^{\alpha\beta} e^{-j\theta_i}; \qquad i = 1 \ldots m \quad (16)$$

where θ_i is the angle of the $i-$th frame of reference and m is the number of inputs.

The following rotation matrices are defined:

$$\Theta_u = diag\left\{e^{-j\theta_1}, e^{-j\theta_2}, \cdots, e^{-j\theta m}\right\} \quad (17)$$

$$u^{dq} = \Theta_u u^{\alpha\beta} \rightarrow u^{\alpha\beta} = \Theta_u^{-1} u^{dq} \quad (18)$$

and:

$$\Theta = diag\left\{e^{-j\theta_1}, e^{-j\theta_1}, e^{-j\theta_2}, e^{-j\theta_2}, \cdots, e^{-j\theta m}\right\} \quad (19)$$

$$x^{dq} = \Theta x^{\alpha\beta} \rightarrow x^{\alpha\beta} = \Theta^{-1} x^{dq} \quad (20)$$

where one or more $\alpha\beta$ state variables are transformed to each dq frame. Therefore:

$$\dot{x}^{dq} = \dot{\Theta} x^{\alpha\beta} + \Theta \dot{x}^{\alpha\beta} \quad (21)$$

$$\Theta \dot{x}^{\alpha\beta} = \dot{x}^{dq} - \dot{\Theta} x^{\alpha\beta} \quad (22)$$

Transforming (15) to the new coordinates:

$$\Theta \dot{x}^{\alpha\beta} = \Theta A x^{\alpha\beta} + \Theta B u^{\alpha\beta} \quad (23)$$

$$\dot{x}^{dq} = \left(\Theta A + \dot{\Theta}\right) x^{\alpha\beta} + \Theta B u^{\alpha\beta} \quad (24)$$

$$\dot{x}^{dq} = \left(\Theta A \Theta^{-1} + \dot{\Theta}\Theta^{-1}\right) x^{dq} + \Theta B \Theta_u^{-1} u^{dq} \quad (25)$$

where $\Theta B \Theta_u^{-1} = B$ if all inputs are local and $\dot{\Theta}\Theta^{-1} = -j\Omega_l$. Ω_l is a diagonal matrix with its elements being the angular speed of each state dq-reference frame ($\omega_i = \frac{d}{dt}\theta_i$):

$$\Omega_l = diag\left(\dot{\theta}_1, \dot{\theta}_1, \dot{\theta}_2, \dot{\theta}_2, \ldots, \dot{\theta}_m\right) \quad (26)$$

Therefore:

$$\dot{x}^{dq} = \left(\Theta A \Theta^{-1} - j\Omega_l\right) x^{dq} + B u^{dq} \quad (27)$$

The local dqi synchronous frame control for each converter will be:

$$\dot{\theta}_i = f_{\theta i}\left(x_{ci}^{dqi}, x_1^{dqi}, x_2^{dqi}, \ldots, x_{ni}^{dqi}\right) \quad (28)$$

$$\dot{x}_{ci}^{dqi} = f_i\left(\theta_i, x_{ci}^{dqi}, x_1^{dqi}, x_2^{dqi}, \ldots, x_{ni}^{dqi}, u_{refi}^{dqi}\right) \quad (29)$$

$$u_i^{dqi} = g_i\left(\theta_i, x_{ci}^{dqi}, x_1^{dqi}, x_2^{dqi}, \ldots, x_{ni}^{dqi}, u_{refi}^{dqi}\right) \quad (30)$$

where θ_i is the angle of the i-th dq reference framce, x_{ci}^{dqi} are the local controller states, u_{refi}^{dqi} are the local input references and $\left(x_1^{dqi}, x_2^{dqi}, \ldots, x_{ni}^{dqi}\right)$ are the local feedback state variables, which, as previously mentioned, are all expressed in the local dqi-frame.

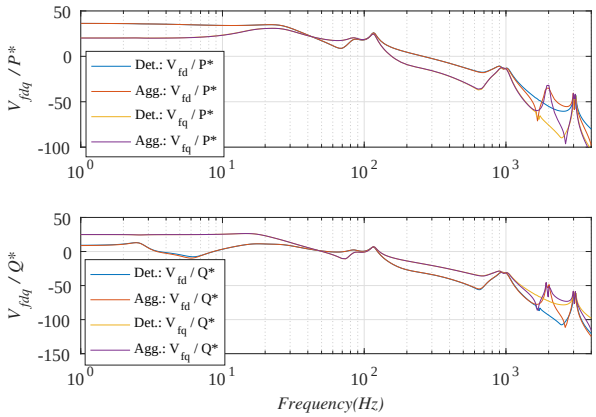

Fig. 4: Frequency response from P^* and Q^* to the DR substation busbar voltage (V_f)

4.1 *Local d-q Controllers*

The grid following PLL dynamics according to (28) to (30), considering the filtering of V_{cqi}:

$$\dot{\theta}_{Ci} = -K_{P,PLL}\widehat{V}_{cqi} - K_{I,PLL}x_{2i} + \omega_0 \quad (31)$$

$$\dot{x}_{2i} = \widehat{V}_{cqi} \quad (32)$$

$$\dot{\widehat{V}}_{cqi} = -\omega_a\widehat{V}_{cqi} + \omega_a V_{cqi} \quad (33)$$

Regarding the Grid Forming wind turbines, the P-V and Q-ω control droops using the filtered active and reactive power will be:

$$\dot{\theta}^*_{Cj} = K_{P,Qm}(\dot{Q}^*_{WTj} + \omega_c\widehat{Q}_{WTj} - \omega_c Q_{WTj}) + \omega_0 \quad (34)$$

$$\dot{\widehat{P}}_{WTj} = -\omega_c\widehat{P}_{WTj} + \omega_c P_{WTj} \quad (35)$$

$$\dot{\widehat{Q}}_{WTj} = -\omega_c\widehat{Q}_{WTj} + \omega_c Q_{WTj} \quad (36)$$

$$\dot{x}_{3j} = P^*_{WTj} - \widehat{P}_{WT} \quad (37)$$

$$V^*_{Cdj} = K_{P,Pm}(P^*_{WTj} - \widehat{P}_{WTj}) + K_{I,Pm}x_{3j} \quad (38)$$

where the i, j subscripts refer to grid following and grid forming WTGs, respectively, ω_a and ω_c are the voltage and power filter cut-off frequencies, x_{2i}, x_{3j} are auxiliary variables and $\widehat{V}_{cqi}$, $\widehat{P}_{WTj}$ and $\widehat{Q}_{WTj}$ are the corresponding filtered variables.

4.2 *Small Signal Analysis*

A small signal analysis is carried out to find up to which extent the design of local controllers is valid for the complete system and the sensitivity to PLL and droop gains. Due to the size of the system, a detailed grid forming string and a detailed grid following string, with 9 WTGs each, have been considered. This approach allows for the model to keep both intra-string and inter-string dynamics. The considered system has 370 states and has been linearised according to Appendix 2.

4.2.1 Response of aggregated and detailed systems: Fig. 4 shows the frequency response of the aggregated and detailed systems. The graph shows the frequency response from the active and reactive power references (P^*, Q^*) to the diode rectifier busbar voltage (V_f). In order to allow the comparison superposition principle has been applied to show the frequency response of the detailed string.

The frequency response shows that both the aggregated and detailed system have almost an identical response up to 1.2 kHz. The overall behaviour of both detailed and aggregated WTGs is very similar in the frequency range of interest, hence, a controller tuning based on aggregated WTGs will give a reasonable approximation to the dynamic response of the detailed system. Nevertheless, discrepancies do exist and a distributed control design should be used if the aggregated tuning does not lead to the expected performance.

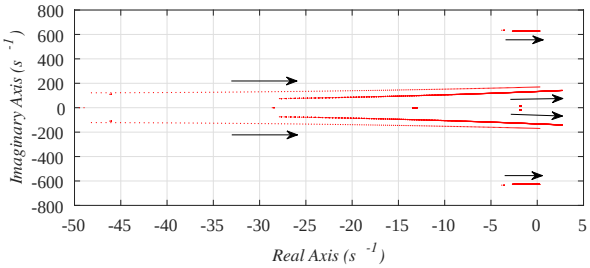

Fig. 5: Root locus when $K_{I,Pm}$ increases from 105 to 630

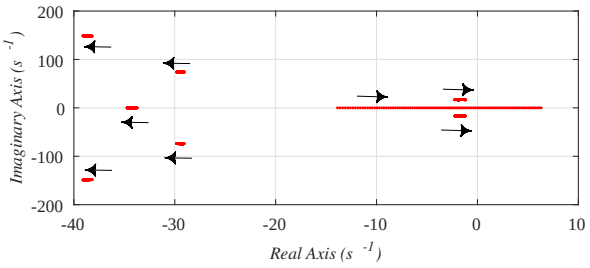

Fig. 6: Root locus when $K_{P,Qm}$ increases from 1 to 1.375

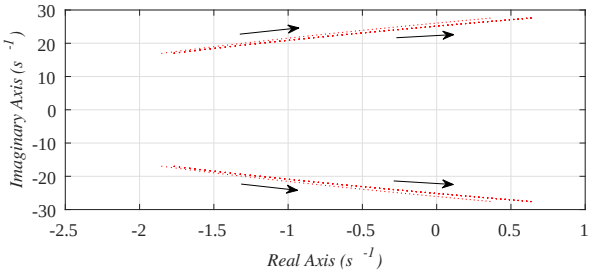

Fig. 7: Root locus when $K_{I,PLL}$ increases from 40 to 120

4.2.2 Sensitivity to PLL and droop gains: Clearly, the grid forming Q-ω droop and the grid following PLL show a very similar structure [27], as their main purpose is grid synchronisation.

Therefore, figs. 5 to 7 show the sensitivity of the detailed grid forming and grid following system to changes in the corresponding PLL and droop gains $K_{I,Pm}$, $K_{P,Qm}$ and $K_{I,PLL}$.

Fig. 5 shows how the position of the dominant poles when $K_{I,Pm}$ increases from 105 to 630 (keeping $K_{P,Qm}$ and $K_{I,PLL}$ at their nominal values). The system shows oscillations around 150 rad/s when the value of $K_{I,Pm}$ exceeds 598.

Fig. 6 shows how the position of the dominant poles when $K_{P,Qm}$ increases from 1 to 1.375 (with constant $K_{I,Pm}$ and $K_{I,PLL}$). The system becomes unstable for $K_{P,Qm} > 1.19$.

Similarly, fig. 7 shows how the position of dominant poles when $K_{I,PLL}$ increases from 40 to 120, while keeping $K_{I,PLL}$ constant. When $K_{I,PLL}$ exceeds 100.2 the WPP becomes unstable, showing a sub-synchronous oscillation of approx. 26 rad/s.

From these figures, it is clear that changes in $K_{I,PLL}$ affect mainly the poles at $s = -1.8 \pm j17$, changes in $K_{I,Pm}$ affect mainly the poles at $s = -30 \pm j70$ and $s = -38 \pm j150$ whereas changes in $K_{K,Qm}$ mainly influence the pole at $s = -14$. Therefore, it is possible to tune these three parameters almost independently in order to modify the damping ratio of the corresponding poles.

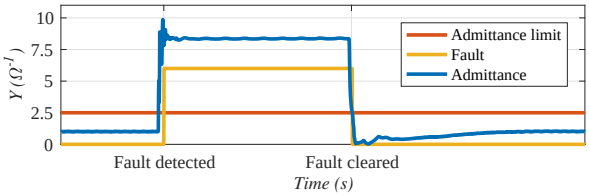

Fig. 8: Off-shore fault detection using impedance measured by WTG.

5 Fault Ride Through

Fault behaviour and recovery is paramount for the correct co-ordination of HVDC-Diode Rectifier connected grid forming and grid following WTGs. This section includes the detailed faul-ride-through study to faults in a grid forming WTG string and also in the off-shore ring-bus.

5.1 Fault-ride-through Strategy

Both the grid forming and the grid following WTGs make use of the control blocks (1) and (2) shown in Fig. 2 and Fig. 3. These control blocks are proposed to improve the system response to off-shore ac-grid faults.

In addition, both types of WTGs implement a short-circuit detection function Y_{fault} using the admittance Y_T which is calculated using local measurements

$$Y_T \angle \varphi = \frac{I_T \angle \theta_{IT}}{V_C \angle \theta_C} \tag{39}$$

When the magnitude of the admittance exceeds a threshold, the WTG considers that a fault has occurred, Fig. 8. The fault signal is used in the control blocks (1), and (2)which are explained as follows.

• Block-(1): V_W^* *dynamic saturation:* During the short-circuit ($Y_{fault} = 1$), the limit of V_W^* is reduced to $\widehat{V}_C + 0.05$ pu, where $\widehat{V}_C$ is the filtered voltage V_C with a time constant of 100 ms. When the fault is cleared, the V_W^* limit increases to 1.1 pu following a 10 pu/s ramp. This ramp is used to improve the transient voltage recovery, as WTGs might detect the fault clearance at different times, depending on the distance to the fault.
• Block-(2): I_W^* *dynamic saturation:* During the short-circuit, the limit of I_W^* is 1.1 pu to provide correct relay protection. At short-circuit clearance (Y_{fault} negative edge) the limit of I_W^* is reduced to 0.05 pu during 25 ms to allow WTGs resynchronization with limited currents. Then it is increased to 1.1 pu at a rate of 10 pu/s.

The fault-ride-through control strategies described previously have been validated using detailed PSCAD simulations. Both grid forming and grid following control strategies have been implemented as digital controllers with a sampling time of 250 μs. For the following tests, the 400 MW OWF_1 consists of grid forming WTGs, whereas the two remaining OWFs of 400 MW each, consist of grid following WTGs. As described previously, each OWF is modeled by a total of 14 WTGs (9 individual WTGs in a single string and further 5 aggregated WTGs for each remaining string in the OWF, see Fig.1).

Several scenarios have been considered to check the integration of grid forming and grid following WTGs during off-shore short-circuits (Fig. 1). The first scenario is a short-circuit at a string of the grid forming wind farm (OWF_1). This scenario is important in order to validate that system remains stable if it loses a sizeable amount of grid forming power.

The second scenario is a short-circuit in one of the ring bus cables, as a worst case scenario.

A third scenario is considered in order to check adequate steady state and fault-ride-through operation without active power generation from grid forming WTGs. The third scenario includes the fault-ride-through response to a cable fault in one of the grid forming strings.

In all three scenarios, the breakers at both ends of the short-circuited cable clear the fault in 200 ms.

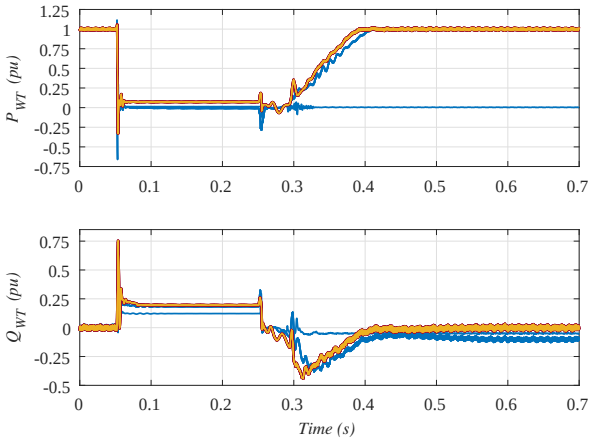

Fig. 9: WTG active and reactive powers during a string short-circuit: OWF_1 (blue), OWF_2 (red), OWF_3 (yellow).

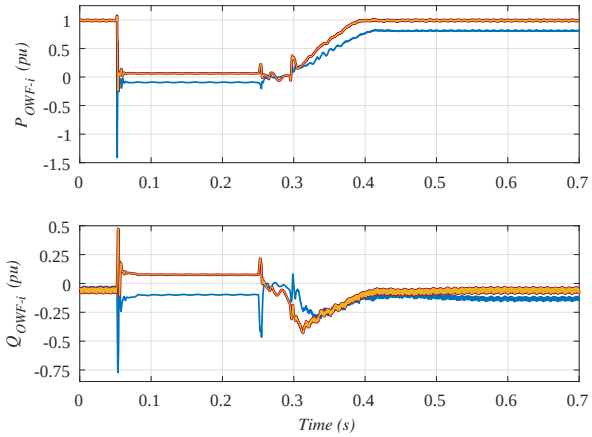

Fig. 10: OWFs active and reactive powers during a string short-circuit: OWF_1 (blue), OWF_2 (red), OWF_3 (yellow).

5.2 Grid Forming OWF String Cable Fault

Figs. 9 to 12 show the behaviour of both grid forming and grid following WTGs during a grid forming OWF string short-circuit. The short-circuit occurs at $t = 50$ ms and is cleared at $t = 250$ ms.

Fig. 9 shows the instantaneous active and reactive powers of each of the grid forming and grid following WTGs. As seen in Fig. 9, at the short-circuit onset, the instantaneous active power peak is higher in WTGs that have the short-circuit nearer. This is because the impedance of the grid, as seen from WTGs, decreases when the short-circuit is closer. Moreover, during the short-circuit, the injected active power is lower for WTGs nearer to the fault as their voltage is smaller while current limits are the same for all WTGs.

Note that, since there is no active power transmitted through the HVDC link and because of the solid fault, most part of the short-circuit current is, effectively reactive, as shown in fig. 9.

When the fault is cleared, the system remains controlled and stable with reduced grid forming power. After approximately 50 ms, active power injection is resumed, hence the DRUs are conducting. Full power transmission is resumed at approx. 150 ms after the fault is cleared.

At the same time, the WTGs in the isolated string also power and bring-up the now islanded string. Note the active power delivered by the islanded WTGs is very small and their reactive power

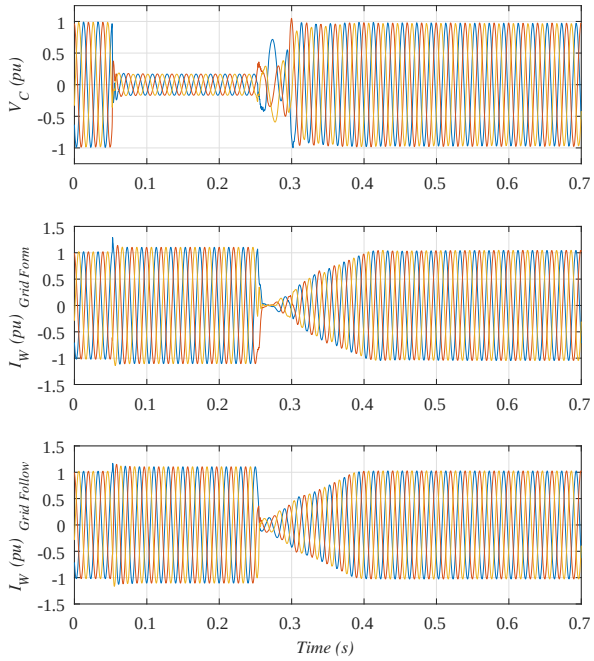

Fig. 11: WTG voltages and currents during string short-circuit.

shows spikes caused by the in-rush current due to the wind turbine transformer saturation, [28].

During recovery, the off-shore ac-grid is over compensated because of the DRU-filters are connected and the active power being transmitted by the DRUs is still zero or very small. Therefore, the WTGs will absorb the reactive power over-compensation until nominal active power transmission is resumed. As DRU filters are rated around 0.4 pu, the grid forming WTGs (one third of installed power) cannot absorb enough reactive power, therefore, the grid following WTGs help restoring the system by absorbing reactive power during the recovery.

Fig. 10 shows the total instantaneous active and reactive powers from each OWF (Fig. 1). The initial power peak is higher in OWF_1 than in the other WPPs, as the short-circuit is at one string of OWF_1. The -1 pu active power surge corresponds to the discharge of cable and DRU filter capacitance and lasts less than 2 ms. However, most of that active power is fed to the short-circuit and the grid forming WTGs do not have to withstand such a large power surge (as seen in fig. 9).

During the short-circuit, clearly OWF_2 and OWF_3 contribute to the short-circuit active and reactive currents. DRU filters absorb around 0.35 pu reactive power, therefore reactive power contribution from all OWFs is required. During fault recovery, grid following WTGs inject maximum allowed reactive current, until the DRU starts conducting. From that point onwards, the WTG reactive power set-point is reduced to its pre-fault value with a 10 pu/s ramp rate (Fig. 10).

Fig. 10 also shows system restoration after the fault is cleared. OWF_1 active power is lower after the fault is cleared as one of its 72 MW (0.18 pu) strings has been disconnected. Therefore total transmitted power is reduced by 72 MW and additional reactive power from the grid-forming WTGs is needed to offset the DRU filter reactive power over-compensation.

Fig. 11 shows the instantaneous voltage V_C and the current I_W of grid forming and grid following WTGs. The voltage of the grid forming and grid following WTGs are similar, so only the voltage of the grid forming is shown.

The voltage distortion after the short-circuit clearance is caused by the breaker arc of each pole being extinguished at the zero crossings of the pole fault current.

The current surge at the beginning of the fault is lower than 1.3 pu during 2 ms, which compares favourably to commercial IGBTs which can withstand peak collector current up to 2 pu during

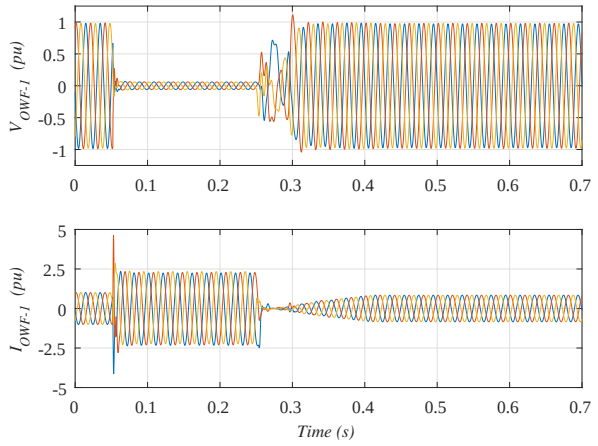

Fig. 12: DRU Platform-1 AC voltages and currents during a string short-circuit.

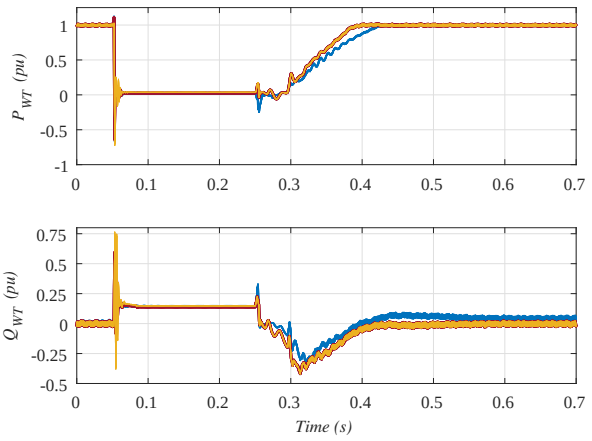

Fig. 13: WTG active and reactive powers during ac-ring-bus short-circuit: OWF_1 (blue), OWF_2 (red), OWF_3 (yellow).

1 ms [29]. Note all WTGs deliver 1.1 pu current during the short-circuit. When the fault is cleared ($t = 0.25$ s), there is a voltage transient due to the sudden increase in system impedance. Moreover, during approx. 50 ms, the WTGs self-synchronize. At $t = 0.33$ ms, the off-shore grid voltage has completely recovered and OWF_1 resumes active power production at $t = 0.37$ ms, i.e. 120 ms after the fault has been cleared. The final OWF_1 current is smaller than its pre-fault current, as one of its strings has been disconnected to clear the fault (see fig. 12).

Fig. 12 shows the voltage at DRU Platform-1 and the current from OWF_1 (Fig. 1). During the short-circuit the voltage drop at DRU Platform-1 is higher than the voltage drop at WTGs (see Fig. 11), because the impedance from the short-circuit to the WTGs (cable plus WTG transformer) is higher than the impedance to the DRU Platform-1 (only the cable). Moreover, the short-circuit current is above 2 pu during the short-circuit, due to the contribution of the other two wind farms.

5.3 Short-Circuit at Off-shore ac-Ring bus

Figs. 13 to 16 show the response of the system to a fault in the off-shore ac-grid ring bus (see Fig. 1).

Figs. 13 and 14 show active and reactive powers response in WTGs and offshore wind farms, respectively, whereas figs. 15 and 16 show instantaneous currents and voltages in WTGs and off-shore wind farms.

The results are very similar to those shown for the string short-circuit, with a much smaller WPP voltage at the DRU platform connection point as the fault is now electrically closer.

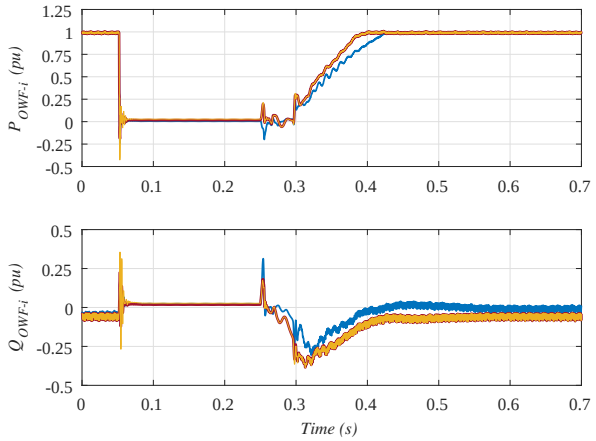

Fig. 14: OWFs active and reactive powers during ac-ring-bus short-circuit: OWF_1 (blue), OWF_2 (red), OWF_3 (yellow).

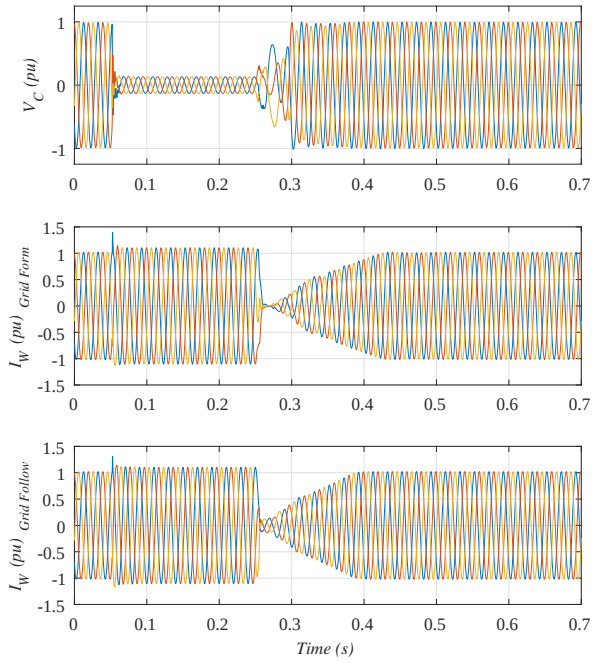

Fig. 15: WTG voltages and currents during ac-ring-bus short-circuit.

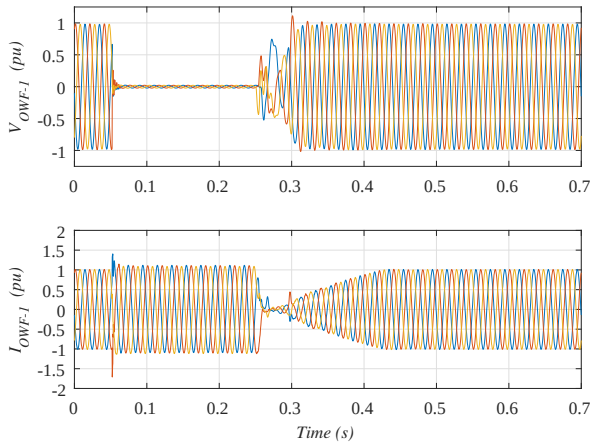

Fig. 16: DRU Platform-1 AC voltages and currents during ac-ring-bus short-circuit.

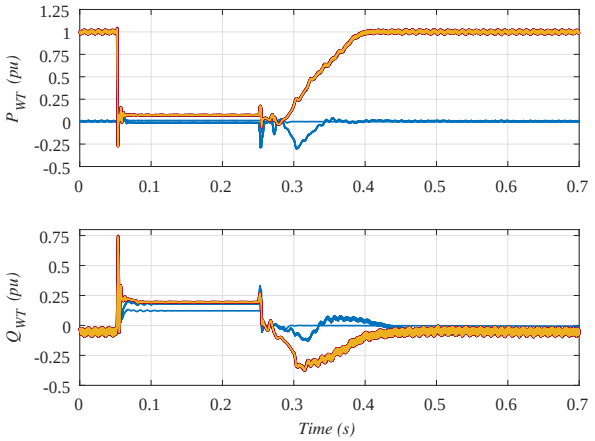

Fig. 17: WTG active and reactive powers during a string fault: OWF_1 (blue), OWF_2 (red), OWF_3 (yellow)

In addition, the cable that connects OWF1 and OWF2 has been disconnected to clear the short-circuit. So, after the short-circuit, the grid forming WTGs produce more reactive power to compensate the contribution of the disconnected cable (see fig. 13).

5.4 Grid Forming WPP String Fault when it is Generating Zero Active Power

As the grid forming WPP is responsible to keep the DRU operational, an important concern is both steady state and fault operation when the grid forming WPP is not generating any active power due to low wind conditions.

Figs. 17 and 18 show the response to a grid forming WPP string fault (fault-1 in fig. 1) when grid forming WTGs are not generating active power.

Fig. 17 shows grid forming and grid following WTG active and reactive powers response, whereas fig. 18 shows WTG instantaneous currents and voltages.

The results show adequate steady state and fault operation. The behaviour in this scenario is similar to the short-circuit when the grid forming WTGs are generating the maximum active power (Figs. 9 to 12). In this scenario one third of the DRU capacitor and filter banks have been disconnected to prevent reactive power over-compensation.

Therefore, it has been shown that adequate fault-rid-through operation is possible with the grid forming WTGs generating only a peak of 100 MW (0.08 pu of rated 1.2 GW) and 40 MVAr (0.03 pu) during voltage recovery.

6 Discussion and Conclusions

This paper has presented the interoperability of grid forming and grid following WTGs when connected to a diode rectifier based HVDC link.

The considered control for the grid forming WTGs does not require communication for proper operation and does not require the use of phase-locked-loops or frequency-locked-loops for their operation.

The small signal stability analysis of the mixed system, considering detailed strings, has been carried out. The comparison of the frequency response of the aggregated and the distributed plants has been carried out, with good agreement in a wide range of frequencies.

It has been shown that an increase in either PLL or droop gains would lead to worse dominant pole damping and even to instability. It has been found that dominant poles are affected independently by either PLL or droop gains.

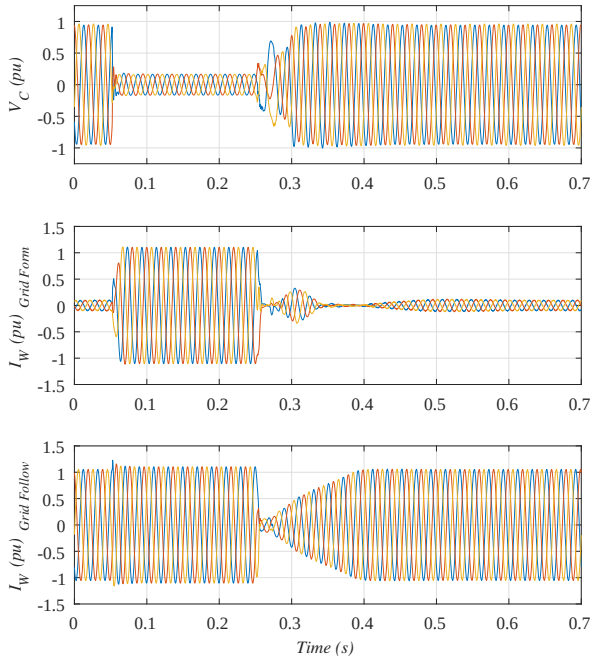

Fig. 18: WTG voltages and currents during a string fault

Particular attention has been paid to adequate joint response during transients. The same fault-ride-through strategy has been implemented in both grid forming and grid following WTGs. Fault onset and fault clearance detection is carried out by the individual WTGs.

The proposed control strategies has been shown to keep wind turbine active, reactive, current and voltage magnitudes within their operational levels during faults.

It has been shown that the system can operate with 328 MW grid forming WTGs and 800 MW grid following WTGs, which represent a percentage of 29% wind forming WTGs with respect to total delivered power.

Furthermore, it has been shown that grid forming WTGs are capable of controlling the off-shore grid even when they are not generating active power, while showing adequate fault response and fault recovery. This is particularly important as it shows that the grid following WPP can operate with very low or no power production in the grid forming WPP.

Acknowledgment

The authors would like to thank the support of the Spanish Ministry of Economy and EU FEDER funds under grants DPI2014-53245-R and DPI2017-84503-R. This project has received funding from the *European Union's Horizon 2020 research and innovation program* under grant agreement No. 691714.

Appendix 1

Table 1 shows the parameters values of the system components. Table 2 shows the parameters values of the control strategies.

Table 1 System Parameters

Wind Turbines
Grid-side converter: 8 MW, 1.2 kVcc, 690 Vac, 50 Hz Grid-side filter: $R_T = 476.1\ \mu\Omega$, $L = 18.94\ \mu$H, $C = 2674\ \mu$F Transformer: 9.2 MVA, 0.69/66 kV, $R_W = 0.004$ pu, $X_W = 0.1$ pu, Saturable
Off-shore ac-grid
WTG to WTG distance: 2 km WTG to ring-bus distance: 4 km Distance between platforms: 10 km String cable sections: C = 150 mm^2, B = 185 mm^2, A = 400 mm^2 String with 8 WTGs: C-C-B-B-B-B-B-A String with 9 WTGs: C-C-B-B-B-B-B-B-A-A
DRU Platform
Filter and compensation filter bank according to [30] Transformer: 215 MVA, 66/43/43 kV, $R_{TR} = 0.004$ pu, $X_{TR} = 0.27$ pu dc-smoothing reactor: 66.67 mH
On-shore full-bridge MMC
MMC: 1400 MW, $\pm$320 kVcc, 370 kVac, 50 Hz MMC arm reactor: 50 mH MMC reactor: 1.25 mH, 1 Ω Transformer: 1400 MVA, 370/230 kV, $X_V = 0.1$ pu

Table 2 System Control Parameters

Common Controls
Current control: $G_{PR,I}$: $K_{P,I}$ = 1.75, $K_{R,I}$ = 360.0; K_V = 0.843
Grid Forming Controls
Voltage control: $G_{PR,V}$: $K_{P,V}$ = 0.28, $K_{R,V}$ = 360.0 Active power control: $G_{PI,Pm}$: $K_{P,Pm}$ = 1.95, $K_{I,Pm}$ = 105.0 Reactive power control: $G_{P,Qm}$: $K_{P,Qm}$ = 1.0
Grid Following Controls
PLL: $G_{PI,PLL}$: $K_{P,PLL}$ = 1.0, $K_{I,PLL}$ = 40.0 Active power control: $G_{PI,Pl}$: $K_{P,Pl}$ = 0.5, $K_{I,Pl}$ = 64.0 Reactive power control: $G_{PI,Ql}$: $K_{P,Ql}$ = 0.5 , $K_{I,Ql}$ = 64.0

Appendix 2. Linearization

This section includes the linearization procedure being carried out for the small signal analysis of the complete system:

$$\dot{x}^{dq} = \Theta A \Theta^{-1} x^{dq} - j\Omega x^{dq} + B u^{dq} \tag{40}$$

$$\dot{\theta}_i = f_{\theta i}\left(x_{ci}^{dqi}, x_1^{dqi}, x_2^{dqi}, \ldots, x_{ni}^{dqi}\right) \tag{41}$$

$$\dot{x}_{ci}^{dqi} = f_i\left(\theta_i, x_{ci}^{dqi}, x_1^{dqi}, x_2^{dqi}, \ldots, x_{ni}^{dqi}, u_i^{dqi}\right) \tag{42}$$

$$u_i^{dqi} = g_i\left(\theta_i, x_{ci}^{dqi}, x_1^{dqi}, x_2^{dqi}, \ldots, x_{ni}^{dqi}, u_{refi}^{dqi}\right) \tag{43}$$

The following vectors are defined: $\theta = (\theta_1, \theta_2, \ldots, \theta_m)^T$, $x_c^{dq} = \left(x_c^{dq1}, x_c^{dq2}, \ldots, x_c^{dqm}\right)^T$, $u_{ref}^{dq} = \left(u_{ref}^{dq1}, u_{ref}^{dq2}, \ldots, u_{ref}^{dqm}\right)^T$.

Also, the following functional vectors are defined:

$$\Omega = (f_{\theta 1}, f_{\theta 1}, f_{\theta 2}, f_{\theta 2}, \cdots, f_{\theta m})^T \tag{44}$$

$$G = (g_1, g_2, g_3, \cdots, g_m)^T \tag{45}$$

$$F = (f_1, f_2, f_3, \cdots, f_m)^T \tag{46}$$

$$F_\theta = (f_{\theta 1}, f_{\theta 2}, f_{\theta 3}, \cdots, f_{\theta m})^T \tag{47}$$

In the steady state operating point:

$$f_{\theta 10} = f_{\theta 20} = \cdots = f_{\theta m0} = \omega_0 \tag{48}$$

And the linearised system will be

$$\Delta\dot{x}^{dq} = \left(\Theta A \Theta^{-1} - j\frac{\partial\left(\Omega x^{dq}\right)}{\partial x^{dq}}\right)\Delta x^{dq} - j\frac{\partial\left(\Omega x^{dq}\right)}{\partial x_c^{dq}}\Delta x_c^{dq} + \left(B - j\frac{\partial\left(\Omega x^{dq}\right)}{\partial u^{dq}}\right)\Delta u^{dq} + \frac{\partial\left(\Theta A \Theta^{-1} x^{dq}\right)}{\partial\theta}\Delta\theta \tag{49}$$

$$\Delta\dot{\theta} = \frac{\partial F_\theta}{\partial x^{dq}}\Delta x^{dq} + \frac{\partial F_\theta}{\partial x_c^{dq}}\Delta x_c^{dq} + \frac{\partial F_\theta}{\partial\theta}\Delta\theta \tag{50}$$

$$\Delta\dot{x}_c^{dq} = \frac{\partial F}{\partial x^{dq}}\Delta x^{dq} + \frac{\partial F}{\partial x_c^{dq}}\Delta x_c^{dq} + \frac{\partial F}{\partial\theta}\Delta\theta + \frac{\partial F}{\partial u^{dq}}\Delta u^{dq} \tag{51}$$

$$\Delta u^{dq} = \frac{\partial G}{\partial x^{dq}}\Delta x^{dq} + \frac{\partial G}{\partial x_c^{dq}}\Delta x_c^{dq} + \frac{\partial G}{\partial\theta}\Delta\theta + \frac{\partial G}{\partial u_{ref}^{dq}}\Delta u_{ref}^{dq} \tag{52}$$

where $\frac{\partial F}{\partial x}$ is the Jacobian of vector field F with respect to vector x evaluated at the steady state operating point.

7 References

1 Blasco.Gimenez, R., Añó.Villalba, S., Rodríguez, J., Morant, F., Bernal, S. 'Uncontrolled rectifiers for hvdc connection of large off-shore wind farms'. In: Power Electronics and Applications, 2009. EPE'09. 13th European Conference on. (IEEE, 2009. pp. 1–8

2 Blasco.Gimenez, R., Añó.Villalba, S., Rodríguez.D'Derlée, J., Morant, F., Bernal.Perez, S.: 'Distributed voltage and frequency control of offshore wind farms connected with a diode-based HVdc link', *IEEE Transactions on Power Electronics*, 2010, **25**, (12), pp. 3095–3105. 00056

3 Blasco.Gimenez, R., Añó.Villalba, S., Rodriguez.D'Derlée, J., Bernal.Perez, S., Morant, F.: 'Diode-based HVdc link for the connection of large offshore wind farms', *IEEE Transactions on Energy Conversion*, 2011, **26**, (2), pp. 615–626. 00047

4 Bernal.Perez, S., Añó.Villalba, S., Blasco.Gimenez, R., Rodriguez.D'Derlee, J.: 'Efficiency and fault ride-through performance of a diode-rectifier- and VSC-inverter-based HVDC link for offshore wind farms', *IEEE Transactions on Industrial Electronics*, 2013, **60**, (6), pp. 2401–2409

5 Blasco.Gimenez, R., Aparicio, N., Añó.Villalba, S., Bernal.Perez, S.: 'LCC-HVDC connection of offshore wind farms with reduced filter banks', *IEEE Transactions on Industrial Electronics*, 2013, **60**, (6), pp. 2372–2380

6 Menke, P.: 'New grid access solutions for offshore wind farms', *EWEA Off-shore*, 2015,

7 Seman, S., Zurowski, R., Christ, T.: 'Investigation of dc converter nonlinear interaction with offshore wind power park system', *EWEA Off-shore*, 2015,

8 Nguyen, T.H., Lee, D.C., Kim, C.K.: 'A series-connected topology of a diode rectifier and a voltage-source converter for an HVDC transmission system', *IEEE TRANSACTIONS ON POWER ELECTRONICS*, 2014, **29**, (4), pp. 1579–1584

9 Yu, L., Li, R., Xu, L.: 'Distributed PLL-based control of offshore wind turbines connected with diode-rectifier-based HVDC systems', *IEEE Transactions on Power Delivery*, 2018, **33**, (3), pp. 1328–1336

10 Li, R., Yu, L., Xu, L.: 'Offshore AC fault protection of diode rectifier unit based HVDC system for wind energy transmission', *IEEE Transactions on Industrial Electronics*, 2018, pp. 1–1

11 Christ, T., Seman, S., Zurowski, R.. 'Power generation facility and method for the operation thereof'. (Google Patents, 2018. uS Patent App. 15/741,777

12 Ramachandran, R., Poullain, S., Benchaib, A., Bacha, S., Francois, B. 'AC grid forming by coordinated control of offshore wind farm connected to diode rectifier based HVDC link - review and assessment of solutions'. In: 2018 20th European Conference on Power Electronics and Applications (EPE'18 ECCE Europe). (, 2018. pp. P.1–P.10

13 Bozhko, S.V., Blasco.Gimenez, R., Li, R., Clare, J.C., Asher, G.M.: 'Control of Offshore DFIG-Based Wind Farm Grid With Line-Commutated HVDC Connection', *Energy Conversion, IEEE Transaction on*, 2007, **22**, (1), pp. 71–78

14 Martínez.Turégano, J., Añó.Villalba, S., Bernal.Perez, S., Blasco.Gimenez, R.: 'Aggregation of type-4 large wind farms based on admittance model order reduction', *Energies*, 2019, **12**, (9), pp. 1730

15 Teodorescu, R., Liserre, M., Rodriguez, P.: 'Grid converters for photovoltaic and wind power systems'. (John Wiley & Sons, 2011)

16 Teodorescu, R., Blaabjerg, F., Liserre, M., Loh, P.C.: 'Proportional-resonant controllers and filters for grid-connected voltage-source converters', *IEE Proceedings-Electric Power Applications*, 2006, **153**, (5), pp. 750–762

17 Timbus, A., Liserre, M., Teodorescu, R., Rodriguez, P., Blaabjerg, F.: 'Evaluation of current controllers for distributed power generation systems', *IEEE Transactions on power electronics*, 2009, **24**, (3), pp. 654–664

18 Yepes, A.G., Freijedo, F.D., Lopez, ., Doval.Gandoy, J.: 'High-performance digital resonant controllers implemented with two integrators', *IEEE Transactions on Power Electronics*, 2011, **26**, (2), pp. 563–576

19 Zmood, D.N., Holmes, D.G.: 'Stationary frame current regulation of PWM inverters with zero steady-state error', *IEEE Transactions on power electronics*, 2003, **18**, (3), pp. 814–822

20 Golestan, S., Guerrero, J.M., Vasquez, J.C.: 'Three-phase PLLs: A review of recent advances', *IEEE Transactions on Power Electronics*, 2017, **32**, (3), pp. 1894–1907

21 Rodriguez, P., Pou, J., Bergas, J., Candela, J.I., Burgos, R.P., Boroyevich, D.: 'Decoupled double synchronous reference frame PLL for power converters control', *IEEE Transactions on Power Electronics*, 2007, **22**, (2), pp. 584–592

22 Vasquez, J.C., Guerrero, J.M., Savaghebi, M., Eloy.Garcia, J., Teodorescu, R.: 'Modeling, analysis, and design of stationary-reference-frame droop-controlled parallel three-phase voltage source inverters', *IEEE Transactions on Industrial Electronics*, 2012, **60**, (4), pp. 1271–1280

23 Guo, Y., Gao, H., Wu, Q., Zhao, H., Østergaard, J., Shahidehpour, M.: 'Enhanced voltage control of VSC-HVDC-connected offshore wind farms based on model predictive control', *IEEE Transactions on Sustainable Energy*, 2018, **9**, (1), pp. 474–487

24 Krause, P.C., Wasynczuk, O., Sudhoff, S.D., Pekarek, S.: 'Analysis of Electric Machinery and Drive Systems'. 2nd ed. (IEEE Press Series in Power Engineering - John Wiley & Sons, Inc., 2002)

25 Guerrero, J.M., Vicuna, L.G.d., Matas, J., Castilla, M., Miret, J.: 'Output impedance design of parallel-connected UPS inverters with wireless load-sharing control', *IEEE Transactions on industrial electronics*, 2005, **52**, (4), pp. 1126–1135

26 Yao, W., Chen, M., Matas, J., Guerrero, J.M., Qian, Z.M.: 'Design and analysis of the droop control method for parallel inverters considering the impact of the complex impedance on the power sharing', *IEEE Transactions on Industrial Electronics*, 2011, **58**, (2), pp. 576–588

27 Zhong, Q.C., Boroyevich, D.: 'Structural resemblance between droop controllers and phase-locked loops', *IEEE Access*, 2016, **4**, pp. 5733–5741

28 CIGRE Study Committee C4: 'Transformer Energization in Power Systems: A Study Guide'. (CIGRE, 2014)

29 'Infineon Technologies, FZ3600R17HE4'. (, 2018

30 Szechtman, M., Wess, T., Thio, C.V.: 'First benchmark model for hvdc control studies', *Electra*, 1991, **Vol. 135**, (Num. 135), pp. 54–73